Smith College

Smith ScholarWorks

7-5-2013

Understanding the origin of the [OI] low-velocity component from T Tauri stars

Elisabetta Rigliaco
University of Arizona

Ilaria Pascucci
University of Arizona

Uma Gorti
SETI Institute

Suzan Edwards
Smith College, sedwards@smith.edu

D. Hollenbach
SETI Institute

Follow this and additional works at: https://scholarworks.smith.edu/ast_facpubs

Part of the Astrophysics and Astronomy Commons

Recommended Citation

UNDERSTANDING THE ORIGIN OF THE [O I] LOW-VELOCITY COMPONENT FROM T TAURI STARS

E. Rigliaco[1], I. Pascucci[1], U. Gorti[2,3], S. Edwards[4], AND D. Hollenbach[2]
[1] Lunar and Planetary Laboratory, The University of Arizona, Tucson, AZ 85721, USA; rigliaco@lpl.arizona.edu
[2] SETI Institute, Mountain View, CA, USA
[3] NASA Ames Research Center, Moffett Feld, CA, USA
[4] Astronomy Department, Smith College, Northampton, MA 01063, USA

ABSTRACT

The formation time, masses, and location of planets are strongly impacted by the physical mechanisms that disperse protoplanetary disks and the timescale over which protoplanetary material is cleared out. Accretion of matter onto the central star, protostellar winds/jets, magnetic disk winds, and photoevaporative winds operate concurrently. Hence, disentangling their relative contribution to disk dispersal requires identifying diagnostics that trace different star–disk environments. Here, we analyze the low-velocity component (LVC) of the oxygen optical forbidden lines, which is found to be blueshifted by a few km s^{-1} with respect to the stellar velocity. We find that the [O I] LVC profiles are different from those of [Ne II] at $12.81\,\mu$m and CO at $4.7\,\mu$m lines pointing to different origins for these gas lines. We report a correlation between the luminosity of the [O I] LVC and the accretion luminosity $L_{\rm acc}$. We do not find any correlation with the X-ray luminosity, while we find that the higher is the stellar far-UV (FUV) luminosity, the higher is the luminosity of the [O I] LVC. In addition, we show that the [O I] $\lambda6300/\lambda5577$ ratio is low (ranging between 1 and 8). These findings favor an origin of the [O I] LVC in a region where OH is photodissociated by stellar FUV photons and argue against thermal emission from an X-ray-heated layer. Detailed modeling of two spectra with the highest S/N and resolution shows that there are two components within the LVC: a broad, centrally peaked component that can be attributed to gas arising in a warm disk surface in Keplerian rotation (with FWHM between $\sim$40 and $\sim$60 km s^{-1}), and a narrow component (with FWHM $\sim$ 10 km s^{-1} and small blueshifts of $\sim$2 km s^{-1}) that may arise in a cool ($\lesssim$1000 K) molecular wind.

Key words: accretion, accretion disks – protoplanetary disks – stars: formation – stars: pre-main sequence – ultraviolet: stars

Online-only material: color figures

1. INTRODUCTION

Planets form in circumstellar disks of gas and dust around young stars. Hence, understanding how protoplanetary disks evolve and disperse is essential to our understanding of the planet formation process. Various mechanisms have been proposed to explain how disks evolve and disperse (see, e.g., Hollenbach et al. 2000 for a review): viscous accretion (e.g., Lynden-Bell & Pringle 1974); MHD winds arising over a narrow range of disk radii near the corotation radius (X-winds; e.g., Shu et al. 2000); MHD winds originating over a large range of disk radii both inside and outside the corotation radius (magnetocentrifugal disk winds; e.g., Königl & Pudritz 2000); photoevaporative winds driven by high-energy photons from the central star (e.g., Clarke et al. 2001); and planet formation (e.g., Hillenbrand 2008). Determining which of these mechanisms dominates requires identifying diagnostics tracing these processes as disks evolve.

High-resolution optical spectroscopy of T Tauri stars (hereafter TTSs) has been crucial in identifying accretion and wind diagnostics. For instance, it is now well established that broad (several hundred km s^{-1}) permitted hydrogen lines mostly trace disk gas falling onto the star in magnetospheric accretion columns (e.g., Calvet et al. 2000 for a review). Forbidden emission lines (such as the bright [O I] line at $\lambda6300$) typically exhibit two distinct components: a high-velocity component (HVC) blueshifted by 50–200 km s^{-1} with respect to the stellar velocity, and a low-velocity component (LVC) typically blueshifted by only $\sim$5–20 km s^{-1} (Hartigan et al. 1995, hereafter HEG; Panoglou et al. 2012). The HVC is unam-

biguously tracing collimated jets that in some cases have been spatially resolved at distances from 50 to several AU from the star (e.g., Hirth et al. 1997; Hartigan et al. 2004).

The origin of the LVC is uncertain. The fact that the line ratios in the LVC are very different from those in the HVC indicates that the two components arise from physically distinct regions (Edwards et al. 1989; Hirth 1994; Hamann 1994; HEG). In addition, the finding that the LVC peak velocities are ordered inversely with their respective critical densities (e.g., $|v_{([S\,II]6731\,Å)}| \geqslant |v_{([O\,I]6300\,Å)}|$) hints at a disk wind origin (HEG). In a disk wind with higher critical densities (like [O I]) form closer to the disk than lines with lower critical densities (like [S II]) and the flow accelerates as it rises from the disk (HEG). However, MHD winds are generally launched at speeds greater than the local Keplerian velocity (e.g., Königl & Salmeron 2011), and the typical radii at which the MHD winds originate are too small to be compatible with the observed small blueshifts in the LVC (see Ferreira et al. 2006 for a review).

More recently, a number of authors have explored the possibility that the LVC of forbidden lines, and in particular the bright [O I] $\lambda6300$ line, traces a thermal photoevaporative wind driven by high-energy photons from the central star (e.g., Font et al. 2004; Ercolano & Owen 2010; Gorti et al. 2011). These authors have considered the different types of stellar radiation that could thermally drive a photoevaporative flow and explain the properties of the [O I] LVC. Stellar EUV photons (13.6 eV $< h\nu \leqslant$ 100 eV) can be easily ruled out since the EUV-heated layer cannot reproduce the large [O I] LVC luminosities that are observed (Font et al. 2004; Hollenbach & Gorti 2009; Ercolano et al. 2009; Owen et al. 2010; Ercolano &

Owen 2010). This is primarily because the EUV-heated layer is mostly ionized and the fraction of neutral gas (including atomic oxygen) is very low. Neutral gas, on the other hand, needs to be relatively hot (∼8000 K) to thermally populate the upper levels of the [O I] transitions. Heating by hard X-rays ($h\nu$ >1 keV) is insufficient as typical gas temperatures achieved are relatively low with $T \sim$ 1000–4000 K (Hollenbach & Gorti 2009; Ercolano et al. 2009; Owen et al. 2010; Ercolano & Owen 2010). A significant flux of soft X-rays (∼0.1–0.3 keV) capable of heating gas to ∼8000 K is needed to produce typical [O I] LVC luminosities. Gas at these temperatures and beyond the gravitational radius[5] is likely to photoevaporate, and the observed [O I] LVC has been attributed to this mechanism (Ercolano & Owen 2010). A detailed study of the nearby disk of TW Hya has raised yet another possibility: that the [O I] emission comes from cooler gas located below a surface layer, and thus the lines trace a bound disk layer where stellar far-UV (FUV) photons (6 eV < $h\nu$ ⩽ 13.6 eV) dissociate OH molecules (Gorti et al. 2011). In this model most of the [O I] emission comes from OH photodissociation (a non-thermal process), and there is only a small contribution from thermal emission. The model accounts for three observational properties of the [O I] lines detected toward TW Hya: (1) a low [O I] λ6300/[O I] λ5577 line ratio, (2) peak velocities centered at the stellar velocity, and (3) small FWHMs of ∼10 km s^{-1} (Pascucci et al. 2011). Photodissociation of OH and H_2O molecules was also proposed by Acke et al. (2005) to explain the origin of the observed [O I] λ6300 luminosity in a sample of Herbig Ae/Be stars observed with high-resolution spectroscopy.

Recently, other near- and mid-infrared lines have been proposed as wind tracers. Using low-resolution spectra, it has been possible to claim that the [Ne II] line at 12.81 μm is an important diagnostic for gas in the disk surface (e.g., Güdel et al. 2010 and references therein). However, ground-based higher resolution observations gave us more information on the line kinematic. Indeed, this line also shows two distinct components like the optical forbidden lines. Similar to the [O I] line, the HVC of the [Ne II] is clearly associated with jets/outflows (it has been also spatially resolved toward one source; see van Boekel et al. 2009), while the profile and peak velocity of the LVC are consistent with a photoevaporative disk wind driven by stellar X-ray/EUV photons (Pascucci & Sterzik 2009; Sacco et al. 2012; Baldovin-Saavedra et al. 2012). Thus, the [Ne II] LVC traces either the EUV-heated or the X-ray-heated disk layer we discussed above in the context of the [O I] LVC (Meijerink et al. 2008; Hollenbach & Gorti 2009; Ercolano & Owen 2010). A less certain diagnostic of disk winds is the fundamental CO $v = 1$–0 emission at 4.7 μm. Spectroastrometry in the CO line (Pontoppidan et al. 2011) shows non-Keplerian motions in a few sources. Those motions are consistent with wide-angle disk winds. Following up on this finding, Bast et al. (2011) and Brown et al. (2013) interpret the small blueshift in the CO peaks (⩽5 km s^{-1}) arising from slow disk winds.

The next step in these studies is to compare different wind diagnostics to understand the structure and evolution of disk winds. If the [O I] lines arise from thermal emission in a mostly neutral photoevaporative wind, similarities with observed [Ne II] emission may be expected if X-rays partially ionize the neon in the mostly neutral gas. [O I] produced as an OH photodissociation product will arise in mainly molecular gas and may be more

correlated with CO emission. Alternately, all three diagnostics may trace different regions of the same wind that is molecular at the base, atomic in the middle, and ionized in its upper layers.

In this paper, we compare the emission from these three proposed wind diagnostics. So far, such a comparison has been carried out only for four disks and has been restricted to the [Ne II] line and optical forbidden lines. Pascucci et al. (2011) analyzed TW Hya, and they found that the [Ne II] and the [O I] lines come from two physically different regions. Baldovin-Saavedra et al. (2012) extended the analysis to three objects. For CoKuTau1 they found that the two lines seem to have the same origin, but the comparison does not allow us to conclusively determine the origin of the lines (disk atmosphere or inner bipolar jet). In FS TauA both the lines appear to come from an EUV/X-ray driven-photoevaporative flow. For V853 Oph, they found that the [Ne II] line is tracing a jet, as only the HVC is detected, while the [O I] lines are compatible with an origin in a photoevaporative wind. According to these previous studies, in three out of four objects analyzed, the [Ne II] and the [O I] lines seem to arise from physically different regions. In this paper we expand these studies in two ways: (1) by extending the comparison to the fundamental CO rovibrational line and (2) by almost tripling the number of objects where different wind diagnostics are analyzed. Focusing on the [Ne II], [O I], and CO, we aim at tracing the ionized, atomic, and molecular layers of such winds covering disk temperatures from ∼10,000 to 1000 K. We also re-analyze already published optical spectra of 30 TTSs with disks (HEG sample) to further constrain the origin of the [O I] emission.

2. DATA COLLECTION

In the following subsections, we present our samples and briefly describe the data reduction and analysis (Sections 2.1 and 2.2). We also provide homogeneously derived effective temperatures, stellar luminosities, and accretion luminosities for all targets (see Sections 2.3 and 2.4). These quantities will be used in Sections 3 and 4 to investigate the origin of the [O I] LVC.

2.1. Sample I

We have assembled a sample of eight TTSs with archival and literature high-resolution optical spectra and either high-resolution N-band (covering the [Ne II] at 12.81 μm) or M-band (covering the CO rovibrational band at 4.7 μm) spectra. We took into account the sources presented in Pascucci & Sterzik (2009), Sacco et al. (2012), and Bast et al. (2011) and selected those whose LVC in either the [Ne II] or CO lines hints at a slow disk wind (blueshifts in the line of a few up to ∼10 km s^{-1}). Table 1 lists the instruments used to acquire the optical spectra, the wavelength coverage, references related to the observing programs, as well as a designation to show if there are [Ne II] and/or CO spectra available. Four out of the eight objects reported in Table 1 (S CrA N, V866 Sco, DR Tau, and VZ Cha) have been observed in the M band by Bast et al. (2011). Two objects (MP Mus and V4046 Sgr) have been observed in the N band (Sacco et al. 2012), and the remaining two objects (RU Lup and TW Hya) have been observed both in the M (Bast et al. 2011) and in the N band (Sacco et al. 2012; Pascucci et al. 2011). As we will see in Section 2.4, except for TW Hya and VZ Cha, the objects observed in the M band are the ones with higher accretion rates.

The optical spectrographs used to observe the targets are VLT/UVES and VLT/FEROS. VLT/UVES was used with

---

[5] The gravitational radius (r_g) is the radius where the thermal speed is equal to the escape speed from the disk.

Table 1
Sample I Sources

Star	R.A.	Decl.	Instrument	Spectral Coverage	[Ne II], CO	Reference
S CrA N	19:01:08.6	−36:57:20.0	UVES	3750–6800 Å	CO	1
V866 Sco	16:11:31.4	−18:38:24.5	UVES	3750–6800 Å	CO	2
DR Tau	04:47:06.2	+16:58:42.9	UVES	3750–7500 Å	CO	1, 3
VZ Cha	11:09:23.8	−76:23:20.8	UVES	4800–6800 Å	CO	4
RU Lup	15:56:42.30	−37:49:15.4	UVES	3500–6800 Å	[Ne II]+CO	1, 4, 5, 6, 7, 10
MP Mus	13:22:07.53	−69:38:12.2	UVES	3300–6800 Å	[Ne II]	7
V4046 Sgr	18:14:10.48	−32:47:34.4	UVES	3500–6800 Å	[Ne II]	8
TW Hya	11:01:51.91	−34:42:17.03	FEROS	3500–9200 Å	[Ne II]+CO	7, 9

References. (1) Petrov et al. 2011; (2) Melo 2003; (3) Fischer et al. 2011; (4) Stempels & Piskunov 2003; (5) Stempels et al. 2007; (6) Stempels & Piskunov 2002; (7) Curran et al. 2011; (8) Stempels & Gahm 2004; (9) Alencar & Batalha 2002; (10) Takami et al. 2001.

different setups, mean resolution $R \sim 70{,}000$ ($\Delta v = 4.3 \, \mathrm{km \, s^{-1}}$), and with slit width between $0\farcs6$ and $1\farcs0$ depending on the observing programs. FEROS is a fiber-fed spectrograph with two fibers, one positioned on the star and the other on the sky (the fiber diameter projected on the sky is $2\farcs7$) from which the sky background is estimated. The mean resolution of the spectrograph is $R \sim 48{,}000$ ($\Delta v = 6.0 \, \mathrm{km \, s^{-1}}$). The FEROS spectra are from Alencar & Batalha (2002).

We reduced the archival VLT/UVES spectra with the ESO/UVES Common Pipeline Library version 3.9.0, which includes bias subtraction, flat fielding, wavelength calibration, and optimal spectrum extraction. To analyze the line profiles, we removed contaminations due to photospheric and terrestrial lines. Following standard procedures (see, e.g., HEG), we first subtracted the terrestrial night-sky emission lines. Then we subtracted telluric absorption lines using telluric standard stars (O-B spectral type) at the same resolution as the target star. Finally, the photospheric absorption lines were subtracted from the target spectra using the spectra of stars without disks that match the spectral type of the target star, and with known rotational velocity. In this last step, we broadened the template spectra to the same rotational velocity of the target star to properly subtract photospheric lines. To define the stellar velocity, we have used the photospheric Ca I line at $\lambda 6439$. An example of our reduction steps applied to the spectrum of V866 Sco is shown in the Appendix (Figure 10).

2.2. Sample II

With the aim of testing whether there is any correlation between the LVC of the [O I] lines and stellar properties, we also re-analyzed already published high-resolution optical spectra from the comprehensive T Tauri survey of HEG. This survey includes 42 sources: 10 stars are non-accreting weak TTSs (WTTSs), while 32 are accreting classical TTSs (CTTSs). In this sample we consider the 30 CTTSs that have published Hα profiles (Beristain et al. 2001), and we exclude DR Tau, which is included in Sample I.

The spectra were collected with the 4 m Mayall telescope at the Kitt Peak National Observatory between 1988 and 1992. The wavelength coverage is 5000–6800 Å in the red and 4000–4950 Å in the blue, with a resolution of $\Delta v \sim 12 \, \mathrm{km \, s^{-1}}$ and a slit width of $1\farcs25$. Details on the data reduction can be found in HEG. The data analysis and the measurements of the equivalent widths (EWs) were done by HEG on the residual line profiles, after subtracting from the target spectra an artificially veiled photosphere of a star with no disk and the same spectral type as the target star, and after shifting the spectra to the rest velocity of the stellar photosphere. We note that Sample II includes objects spanning over the entire accretion luminosity range for solar-mass TTSs (see Section 2.4).

2.3. Stellar Parameters

Stellar parameters for the Sample I and Sample II sources are listed in Tables 2 and 3, respectively.

Effective temperatures and stellar luminosities for the Sample I sources were computed using spectral types (SpT), I-, R-, or V-magnitudes, and extinctions found in the literature. In particular, stellar luminosities have been computed from the dereddened I-band magnitude and the bolometric correction corresponding to the assigned SpT (as reported by Luhman 1999). When the I-band magnitude was not available, we used in order R- or V-band magnitudes, taking into account the corresponding extinction law (Mathis 1990). The uncertainty in the SpT of about half a subclass translates into a ± 70 K uncertainty on the stellar effective temperature. Uncertainties in the stellar luminosity (L_*) depend on the adopted bolometric correction/temperature; I-, V-, or R-magnitude values (known to within ~ 0.2 mag); the error on the extinction, which is $\sim 20\%$ in a typical TTS (Hartigan et al. 1991); and the distance of the source. We estimate a typical uncertainty in the luminosity of ~ 0.5 dex. Stellar masses (M_*) are estimated from the location of the sources in the H-R diagram using Siess et al. (2000) evolutionary tracks. Stellar radii are estimated from stellar luminosities and effective temperatures. The determination of stellar masses and radii is also affected by the distance uncertainty; typical errors on these parameters are ~ 0.05 dex.

For the Sample II sources, we have used the luminosities and the effective temperatures reported in HEG, but we have recomputed the stellar masses using the evolutionary tracks of Siess et al. (2000) for consistency with the Sample I sources (see Table 3). In Tables 2 and 3, we have marked with a single asterisk the multiple systems, and with a double asterisk the systems where two components have a separation smaller than $\sim 0\farcs6$ (half of the slit width employed by HEG; see references to Tables 2 and 3). We note that only 5 out of the total 38 objects (Sample I + Sample II) are binaries closer than $\sim 0\farcs6$.

2.4. Accretion Luminosities

Accretion luminosities (L_{acc}) for the Sample II stars were first computed by HEG from the "veiling"[6] of stellar absorption features at optical wavelengths, basically measuring the hot continuum excess produced by the accretion shock at the stellar

---

[6] The veiling is defined as $(\mathrm{EW}_{\mathrm{true}}/\mathrm{EW}_{\mathrm{meas}}) - 1$, where $\mathrm{EW}_{\mathrm{true}}$ is the EW of the absorption line when no veiling is observed and $\mathrm{EW}_{\mathrm{meas}}$ is the measured EW.

Table 2
Stellar Parameters for the Sample I Sources

Star	$\log L$ $(L_\odot)$	$\log T$ (K)	R_* $(R_\odot)$	M_* $(M_\odot)$	Hα EW (Å)	$\log L_{\rm acc}$ $(L_\odot)$	$V_{\rm mag}$	A_V	$\log L_{\rm [O I]LVC}$[a] $(L_\odot)$	Distance (pc)	Reference
S CrA N*	−0.036	3.681	1.38	1.20	80.0	−0.08	11.59	1.0	−4.05	130	1
V866 Sco N*	0.689	3.648	3.71	1.35	103.1	0.89	12.05	2.9	−3.37	125	1
DR Tau	0.063	3.608	2.17	0.75	78.7	0.45	11.43	1.6	−4.15	140	2
VZ Cha	−0.133	3.623	1.61	0.95	40.0	−1.10	12.94	1.9	−5.23	103	3
RU Lup	0.076	3.602	2.27	0.69	100.3	−0.29	11.44	0.1	−4.47	140	4
MP Mus	0.057	3.702	1.40	1.23	19.5	−1.34	10.44	0.17	−4.96	86	5
V4046 Sgr**	−0.281	3.628	1.33	0.99	42.0	−1.30	10.68	0.0	−5.55	73	6
TW Hya	−0.601	3.591	1.09	0.64	185.8	−1.15	11.27	0.0	−5.32	51	7

Notes. *Binary systems with separation ∼1″4 (Ghez et al. 1993, 1997a; Reipurth & Zinnecker 1993). **Spectroscopic binary (Stempels & Gahm 2004).
[a] [O I] LVC λ6300 luminosity.
References. (1) Prato et al. 2003; (2) Muzerolle et al. 2003; (3) Luhman 2007; (4) Herczeg et al. 2005; (5) Cortes et al. 2009; (6) Donati et al. 2011;
(7) Alencar & Batalha 2002.

Table 3
Stellar Parameters for the Sample II Sources

ID	Star	$\log L$[a] $(L_\odot)$	$\log T$[a] (K)	R_*[b] $(R_\odot)$	M_*[b] $(M_\odot)$	Hα EW[c] (Å)	$\log L_{\rm acc}$ $(L_\odot)$	$V_{\rm mag}$[a,d]	A_V[a]	$\log L_{\rm [O I]LVC}$[a] $(L_\odot)$	$\log L_X$ $(L_\odot)$
1	AA Tau	−0.190	3.58	1.73	0.53	76.9	−0.65	11.66	1.3	−3.94	−3.39[e]
2	AS 353A*	0.570	3.643	3.15	1.22	54.6	−0.10	10.36	2.1	−3.59	⋯
3	BP Tau	−0.060	3.602	1.71	0.70	49.0	−0.58	11.06	1.0	−4.80	−3.43[e]
4	CI Tau	0.020	3.602	2.10	0.69	70.6	−0.35	11.07	2.3	−4.61	−4.23[f]
5	CW Tau	0.332	3.672	2.12	1.60	276.7	1.79	8.96	3.4	−2.69	−3.17[f]
6	CY Tau	−0.330	3.602	1.56	0.71	38.9	−2.04	13.25	0.1	−5.21	−4.08[e]
7	DD Tau**	−0.260	3.498	2.41	0.23	145.1	−0.56	12.21	1.9	−3.89	−4.06[f]
8	DE Tau	0.030	3.533	2.87	0.32	71.2	−0.57	11.45	1.5	−4.71	−4.45[e]
9	DF Tau**	0.310	3.544	3.72	0.36	71.9	−0.16	10.78	1.3	−3.73	<−4.96[f]
10	DG Tau	0.240	3.643	3.03	1.19	71.2	0.90	8.97	3.2	−2.63	⋯
11	DK Tau*	0.230	3.602	2.02	0.69	11.5	−1.15	10.45	2.0	−4.17	−3.74[f]
12	DL Tau	−0.170	3.58	1.84	0.53	121.7	−0.16	11.35	1.7	−4.70	⋯
13	DN Tau	0.030	3.602	2.10	0.69	17.8	−1.34	11.23	1.1	−4.43	−3.52[e]
14	DO Tau	0.050	3.58	2.31	0.52	75.6	0.51	9.70	4.6	−3.63	<−4.16[f]
15	DQ Tau**	−0.020	3.602	1.85	0.69	61.6	−0.66	11.45	2.1	−3.81	⋯
16	DS Tau	0.130	3.69	1.55	1.36	28.4	0.23	9.70	2.2	−4.31	⋯
17	FM Tau	−0.650	3.498	1.50	0.21	74.3	−1.53	13.10	1.2	−5.22	−3.52[e]
18	FP Tau	−0.550	3.477	1.89	0.17	24.8	−2.72	13.91	0.0	−5.51	<−3.89[f]
19	GG Tau**	0.170	3.58	2.66	0.52	45.0	−0.66	11.10	1.25	−4.55	<−4.98[f]
20	GI Tau*	0.070	3.58	2.32	0.52	12.8	−1.65	11.39	1.7	−4.57	−3.66[e]
21	GK Tau*	0.050	3.602	2.12	0.69	17.6	−1.56	11.59	0.78	−4.70	−3.56[e]
22	GM Aur	0.230	3.602	2.02	0.69	110.5	−0.57	11.93	0.10	−4.92	−3.75[e]
23	HK Tau*	−0.040	3.602	1.83	0.69	49.5	−0.39	10.75	5.0	−4.18	−4.44[f]
24	HN Tau*	−0.560	3.602	1.14	0.77	90.8	−0.94	12.33	1.9	−3.71	<−3.88[e]
25	LkCa 8	−0.390	3.58	1.45	0.54	7.9	−2.79	12.79	0.25	−4.92	⋯
26	RW Aur**	0.360	3.662	2.31	1.51	70.0	0.94	8.89	2.2	−3.65	⋯
27	UY Aur*	0.120	3.58	2.45	0.52	76.7	−0.29	11.07	1.3	−3.93	⋯
28	UZ Tau E*	0.440	3.553	4.22	0.39	70.4	0.12	10.28	2.8	−3.34	−4.74[e]
29	V836 Tau	−0.260	3.602	1.58	0.70	2.4	−3.23	12.23	0.9	−4.95	<−3.58[f]
30	YY Ori	0.332	3.602	2.64	0.68	25.9	0.07	11.85	1.9	−3.61	⋯

Notes. *Binary systems with separation larger than 0″6. **Binary systems with separation smaller than 0″6 (Mathieu et al. 1997; Silber et al. 2000;
White & Ghez 2001).
[a] Stellar luminosities, effective temperatures, V-magnitude, extinctions (A_V), and [O I] LVC λ6300 luminosities as published by HEG.
[b] Masses and radii have been recomputed considering the Siess et al. (2000) evolutionary tracks.
[c] Hα equivalent widths as published by Beristain et al. (2001).
[d] Dereddened V-magnitude.
References. [e]Güdel et al. 2007; [f]Stelzer & Neuhäuser 2001.

surface. Recent studies have found that the luminosity of gas lines produced in magnetospheric accretion columns (e.g., the hydrogen recombination lines Hα, Hβ, Paγ, and Paβ among others) correlates with the accretion luminosity ($L_{\rm acc}$; see, e.g., Herczeg & Hillenbrand 2008; Rigliaco et al. 2012 and references therein). In the wavelength range covered by the Sample I

observations, we have been able to obtain an estimate of the accretion luminosity based on the Hα and Hβ line luminosities. However, for the Sample II objects only the Hα line profiles and EWs have been published in the literature (Beristain et al. 2001). Thus, even if the $\log L_{\rm acc}$–$\log L_{\rm Hβ}$ relationship has been found to have a smaller scatter than the $\log L_{\rm acc}$–$\log L_{\rm Hα}$

Table 4
Oxygen Line Parameters Using a Gaussian Fit to the LVC

Star	Sample	EW$_{[O I]6300}$ (Å)	EW$_{[O I]5577}$ (Å)	FWHM[a] (km s^{-1})	v_{peak}[a, b] (km s^{-1})	i (°)	Reference[c]
S CrA N*	I	0.83 (0.09)	0.15 (0.04)	105.5 ± 8.8	−22.3 ± 2.0	...	...
V866 Sco*	I	1.13 (0.10)	0.26 (0.05)	20.2 ± 0.7	−2.1 ± 0.7	25	1
DR Tau	I	0.28 (0.06)	<0.04	14.1 ± 2.7	−0.2 ± 0.7	37	2
VZ Cha	I	0.13 (0.04)	<0.04	22.0 ± 6.2	−3.5 ± 1.5	...	...
RU Lup*	I	0.54 (0.08)	0.10 (0.06)	21.3 ± 15.8	−6.4 ± 1.6	10	3
MP Mus	I	0.17 (0.03)	<0.04	42.6 ± 13.6	−6.8 ± 2.0	30	4
V4046 Sgr	I	0.09 (0.04)	<0.03	47.1 ± 8.4	−0.6 ± 2.0	35	5
TW Hya	I	0.53 (0.06)	0.09 (0.05)	8.2 ± 0.6	−0.0 ± 0.7	7	6
AS 353A	II	0.39 (0.02)	<0.12	42.8$^{+15.0}_{-25.0}$	−7.0[d]	60	7
CW Tau	II	4.3 (0.07)	1.37 (0.06)	44.1 ± 1.5	−6.0[d]	80	8
CY Tau	II	0.37 (0.05)	0.09 (0.04)	40.5 ± 6.6	−3.0[d]	52	9
DF Tau	II	1.27 (0.04)	0.33 (0.03)	34.8 ± 2.0	−4.0[d]	63	10
DN Tau	II	0.43 (0.03)	0.06 (0.03)	55.7 ± 6.3	−9.0[d]	78	9
DQ Tau	II	2.17 (0.04)	0.38 (0.03)	45.1 ± 1.1	−13.0[d]	35	11
FM Tau	II	0.45 (0.05)	0.34 (0.05)	57.6 ± 6.9	−3.0[d]	70	12
GG Tau	II	0.28 (0.02)	0.05 (0.03)	28.3 ± 7.0	−3.0[d]	37	13
GK Tau	II	0.31 (0.03)	0.10 (0.04)	51.1 ± 5.6	−4.0[d]	23	14
GM Aur	II	0.25 (0.04)	0.04 (0.04)	28.9 ± 8.5	+1.0[d]	45	9
UY Aur	II	1.16 (0.02)	0.13 (0.02)	38.8 ± 5.9	−6.0[d]	42	15
YY Ori	II	0.57 (0.08)	0.20 (0.04)	59.2 ± 6.0	−15.0[d]	...	...

Notes.
[a] FWHMs and peak velocities (in the stellocentric reference frame) are from fits to the [O I] λ6300 line except for S CrA N, V866 Sco, and RU Lup (stars with *), where they refer to the [O I] λ5577 line. This choice is motivated by the contamination of the HVC in the [O I] λ6300 LVC (see Figure 1).
[b] The error on the peak centroids for the Sample II objects is ±2 km s^{-1}, as reported by HEG.
[c] Reference is for the disk inclination.
[d] Peak velocities for the Sample II objects are from HEG.

References. (1) Andrews et al. 2010; (2) Isella et al. 2009; (3) Stempels & Piskunov 2002; (4) Kastner et al. 2010; (5) Kastner et al. 2008; (6) Qi et al. 2004; (7) Davis et al. 1996; (8) White & Ghez 2001; (9) Kitamura et al. 2002; (10) Ghez et al. 1997b; (11) Guilloteau et al. 2011; (12) Furlan et al. 2006; (13) Pietu et al. 2011; (14) Weaver 1986; (15) Close et al. 1998.

relationship (Herczeg & Hillenbrand 2008; Fang et al. 2009; Rigliaco et al. 2012), we will use the Hα lines, obtained simultaneously with the [O I] lines, to recompute accretion luminosities consistently for both Sample I and Sample II objects. The errors introduced by considering the Hα line are, qualitatively, a factor of two larger than the errors we would have on the accretion luminosities using the Hβ line.

To measure L_{acc}, we use the most recent relation obtained by Rigliaco et al. (2012) from a sample of low-mass stars and brown dwarfs in the Taurus-Molecular Cloud, in the young open cluster IC 348, and in the σ Orionis cluster:

$$\log \frac{L_{acc}}{L_\odot} = (2.99 \pm 0.16) + (1.49 \pm 0.05) \times \log \frac{L_{H\alpha}}{L_\odot}. \quad (1)$$

In the mass range considered here, this relation is consistent with those found by other groups (Herczeg & Hillenbrand 2008; Fang et al. 2009). To compute the Hα luminosity ($L_{H\alpha}$), we first measure the Hα EW by integrating below the entire line. Then, we use literature V-band magnitudes for the continuum and the extinction values listed in Tables 2 and 3 to obtain $L_{H\alpha}$. We note that we prefer to rely on L_{acc} rather than on mass accretion rates because computing the latter requires determining stellar masses and radii which add additional uncertainties. Moreover, it requires making additional assumptions about poorly constrained disk properties (see, e.g., Gullbring et al. 1998).

2.5. [O I] Line Profile Characterization

To characterize the LVC of the [O I] lines for the Sample I objects, we compute the EWs and associated uncertainties using a Monte Carlo approach. We add a normally distributed noise at each wavelength with an amplitude equal to the flux uncertainty at that wavelength. We then make 1000 realizations of the spectra and EW measurements and take as resulting EW and uncertainty the mean and standard deviation of the distribution (see Pascucci et al. 2008 for further details on the procedure). Five out of the eight Sample I objects show a clear LVC in the [O I] λ6300 line. Two out of eight objects (namely SCrA N and RU Lup[7]) have an HVC that strongly compromises the LVC, while in one object (V866 Sco[3]) the LVC is slightly compromised by the HVC (we note that the HVC is always more pronounced in the [O I] λ6300 than in the λ5577 transition; see also HEG). For these three objects we compute the EW of the LVC integrating over the portion of the spectrum between −60 km s^{-1} and +60 km s^{-1}, following the same method used by HEG. For all the Sample I objects we also measure line luminosities from the line EWs and the total dereddened flux, assuming the distances, magnitudes, and extinctions listed in Table 2. Finally, we provide two additional values to characterize the line profile: the velocity at which the emission peaks (v_{peak})[8] and the width of the profile at half of the peak emission (FWHM, see Table 4).

Table 4 summarizes our measurements. From this table, we omit the [O I] λ6363 EWs because they are always one-third of the [O I] λ6300 EWs, as expected from the Einstein coefficients

---

[7] These are classified disk wind sources by Bast et al. (2011) based on the CO $v = 1$–0 profile.
[8] The profiles cannot be well reproduced by a single Gaussian; therefore, we obtained the peak centroid by averaging the two consecutive velocity values where the emission peaks.
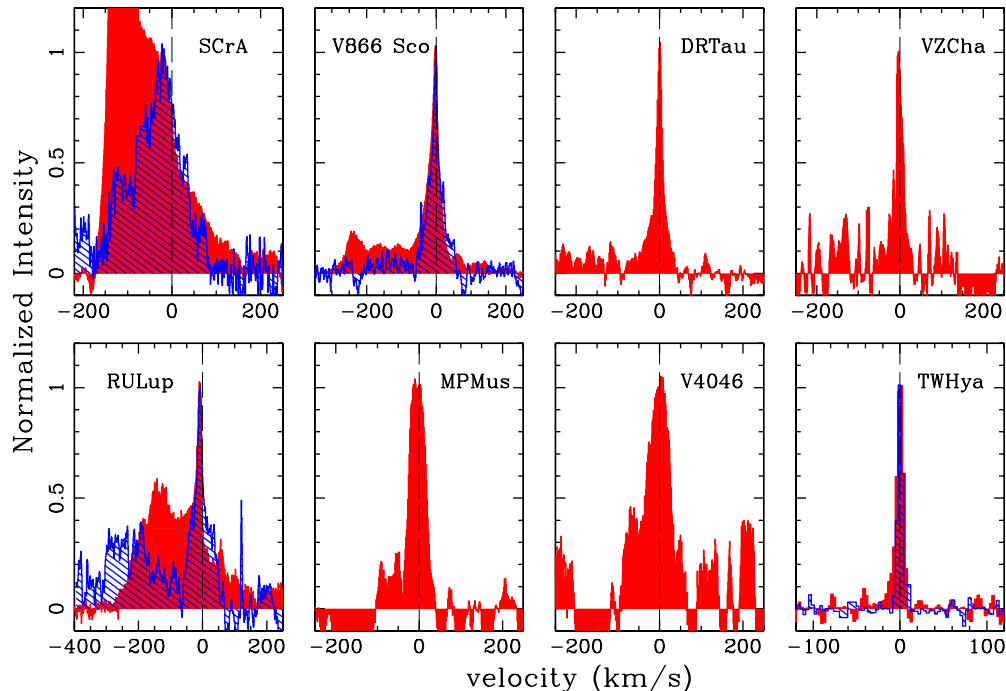
Figure 1. [O I] line profile comparison. The red area represents the profile of the [O I] at λ6300, while the blue shaded area is the [O I] λ5577 line profile. Profiles have been scaled to the peak of the [O I] λ6300 LVC to highlight any difference in the shifts and/or shapes of the two lines. Note that the [O I] λ5577 line is not detected (hence not shown) toward DR Tau, VZ Cha, MP Mus, and V4046 Sgr. Also note that the SCrA N profile has been scaled to the peak of the [O I] λ5577 line.

(A color version of this figure is available in the online journal.)

and energy levels. When the [O I] λ5577 is also detected (in half of the Sample I objects), and the HVC does not contaminate the LVC at low radial velocities, its FWHM and peak centroid are similar to those of the [O I] λ6300 line. As such, we report only the FWHM and centroid of the [O I] λ6300 line in Table 4 for the objects with an LVC well separated from the HVC. In the other cases (SCrA N, RU Lup, and V866 Sco), we report the FWHM and centroid of the [O I] λ5577 line.

For the Sample II objects, we use the luminosities of the [O I] λ6300 line obtained by HEG (Table 5 in their paper and the second-to-last column of Table 3 of this paper). We use the HEG subsample of Sample II objects where the HVC and the LVC components can be well separated (as defined by HEG, and as reported in their Table 8). We report this subsample of objects in Table 4. From the original selection done by HEG we have excluded DGTau, because in this object the [O I] LVC is clearly affected by the presence of the HVC, and DRTau, which is included in our Sample I sources. For these 12 objects, we report in Table 4 the peak velocities as reported in Table 8 of HEG, and we computed the FWHM with the same method described above. We tested that our procedure of measuring v_{peak} is consistent with the one used by HEG.

3. OBSERVATIONAL RESULTS

In the following, we briefly describe our main observational results which stem from the comparison of [O I] line profiles to those of [Ne II] and CO (Sample I sources; Section 3.1) and from trends between the [O I] line luminosities, FWHMs, and peak centroids with stellar parameters (Sample I and II sources; Section 3.2).

3.1. Sample I: Line Profile Comparison

To investigate the origin of the [O I] LVC, we start by analyzing its line profile. A visual comparison of the [O I] λ6300
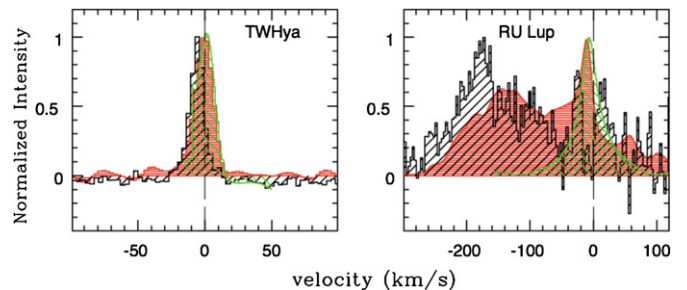

Figure 2. CO (green), [Ne II] (black), and [O I] λ6300 (red) line profile comparison.

(A color version of this figure is available in the online journal.)

and [O I] λ5577 lines is provided in Figure 1. In three out of the four objects where both the [O I] lines are detected (V866 Sco, DR Tau, and TW Hya), this comparison shows that the LVC of the [O I] λ6300 and [O I] λ5577 lines has similar profiles, suggesting that they trace gas with analogous properties (temperature and density), and likely the same region around the star. A similar result can be inferred from the subsample of HEG sources with distinct LVC and HVC components (see their Table 8 and the peak centroids reported for CW Tau, DF Tau, DR Tau, and UY Aur).

Next, we compare the profiles of the strongest of the [O I] lines, that at λ6300, with those of the [Ne II] (tracing unbound gas) and/or CO rovibrational lines, in which the bulk component is mostly coming from the disk (Najita et al. 2003; Salyk et al. 2011; see Figures 2–4). For this comparison, we have degraded the spectra to the lowest resolution spectrum by Gaussian convolution and have normalized the peak intensities to unity.

Figure 2 shows the two Sample I objects where all three gas diagnostics considered here are observed: TW Hya and RU Lup.
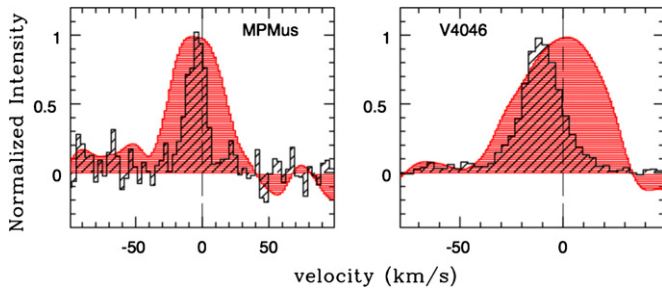
Figure 3. [Ne II] (black) and [O I] λ6300 (red) line profile comparison.
(A color version of this figure is available in the online journal.)

The [O I] λ6300 and the CO rovibrational profiles of TW Hya are symmetric and centered at the stellar velocity, while the [Ne II] line is blueshifted by ∼5 km s^{-1} and asymmetric (see Pascucci et al. 2011 for a detailed analysis). RU Lup shows a complex [O I] profile with blended HVC and LVC components, a CO single-peaked profile less blueshifted than the [O I] LVC, and an [Ne II] line dominated by the HVC (the LVC is likely not detected; see Sacco et al. 2012).

Figure 3 shows the comparison between the [O I] λ6300 and the [Ne II] line profiles for MP Mus and V4046 Sgr. In both sources, the [O I] λ6300 line is broader than the [Ne II] line and coincident with (in MP Mus) or less blueshifted than (in V4046 Sgr) the [Ne II] line.

Finally, Figure 4 shows the comparison of the oxygen and the CO rovibrational lines for the remaining four Sample I objects. We use as a reference transition the [O I] λ6300 line for all sources except for SCrA N, for which we prefer to use the [O I] λ5577 transition because it is less contaminated by the HVC. The [O I] and CO profiles are quite different from each other, and there is no trend in their FWHMs. For VZ Cha, V866 Sco, and SCrA N, the CO line is less blueshifted than the

[O I] λ6300 line. Note that in the first two sources CO appears marginally *redshifted* with respect to the stellar velocity. For DR Tau, the [O I] line is centered at the stellar velocity while the CO line may be slightly blueshifted: Bast et al. (2011) report a peak centroid for the narrow component of −3.2 ± 2 km s^{-1}.

In spite of the diversity in the line profiles, the following trends seem to emerge: (1) the [O I] LVC is broader and less blueshifted than the [Ne II] line; (2) the [O I] LVC is more blueshifted than the CO line; (3) their FWHMs do not follow a simple trend. These preliminary trends are consistent with a scenario in which the [Ne II] line traces mostly the upper surface of a photoevaporative wind at larger radii than the CO and the [O I] lines, which either probe bound gas in the disk or probe lower layers of the [Ne II] wind. These trends are opposite to what is predicted by the models of Ercolano & Owen (2010), where the [O I] lines present a larger blueshift than [Ne II] lines in primordial (not gapped) disks (see Section 4 for more details). In these models, the Ne^{+} is produced by ∼1 keV X-rays in mostly neutral gas, and the [Ne II] arises from somewhat cooler gas than the soft X-ray-heated gas producing the [O I]. Thus, the [O I] emitting region is located higher up in the accelerating flow than the [Ne II] emitting region. A larger sample size is definitively needed to confirm these trends and test this scenario. We will further discuss the [O I] line profiles in Sections 3.2.3 and 3.2.4.

3.2. Samples I and II

To further investigate the origin of the [O I] LVC, we will consider the two samples collected here (the 8 TTSs from Sample I and the 30 TTSs from Sample II) in Sections 3.2.1 and 3.2.2. To analyze the kinematics of the [O I] LVC (Section 3.2.3), we will use the whole Sample I and a subsample of Sample II, where the HVC and the LVC components can be well separated, as defined by HEG (see also Table 4).
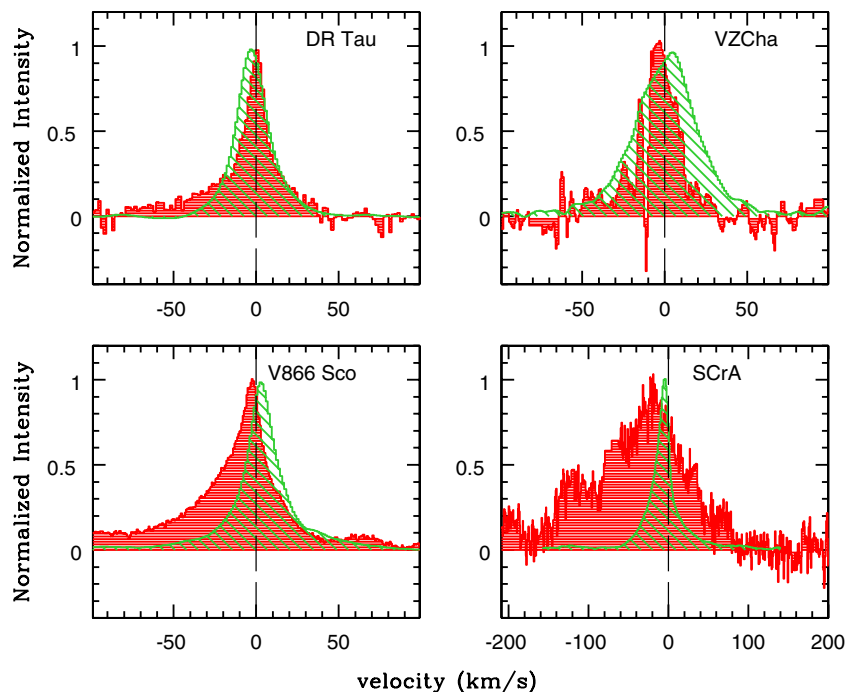

Figure 4. CO (green) and [O I] λ6300 (red) line profile comparison. For SCrA N (bottom right panel), the CO is compared with the [O I] λ5577 line instead of the [O I] λ6300 line.
(A color version of this figure is available in the online journal.)
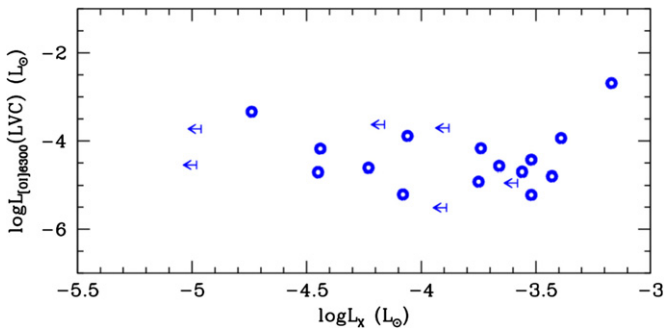
Figure 5. [O I] luminosity vs. X-ray luminosity for the subsample of 21 Sample II objects with X-ray luminosities (L_X) found in the literature.

(A color version of this figure is available in the online journal.)

3.2.1. Correlations with Stellar Properties

We have searched for correlations between the [O I] LVC line luminosity ($L_{\rm [O\,I]LVC}$) and stellar properties for the complete Sample I and II objects (38 objects in total).[9] We report no correlation between $L_{\rm [O\,I]LVC}$ and the stellar luminosity or mass (L_* and M_* in Tables 2 and 3). We also find no correlation between $L_{\rm [O\,I]LVC}$ and the X-ray luminosity L_X for the subsample of 21 Sample II objects (Stelzer & Neuhäuser 2001; Güdel et al. 2007; Figure 5). Instead, we identify a correlation between $L_{\rm [O\,I]LVC}$ and the stellar accretion rate $L_{\rm acc}$ (see Figure 6, top panel). We quantify this correlation by computing a linear least-squares fit in the log scale:

$$\log L_{\rm [O\,I]LVC} = (0.52 \pm 0.07) \times \log L_{\rm acc} - (3.99 \pm 0.09). \quad (2)$$

We note that the HVC, which is associated with jets/outflows, follows a different relation (see Figure 6, top panel) and decreases steeply for low accretion luminosities. Figure 6 (bottom panel) shows that the LVC dominates the [O I] luminosity over a broad range of $L_{\rm acc}$ after the accretion luminosity has decreased below $\sim 1\ L_\odot$. Even for high accretors, the LVC contributes more than 20% to the total [O I] luminosity. A similar behavior was found by HEG when comparing average line profiles as a function of near-infrared colors, a proxy for mass accretion rates (see their Figure 11).

Recently, Yang et al. (2012) found that $L_{\rm acc}$ does not correlate with L_X but correlates tightly with the total FUV luminosity ($L_{\rm FUV}$). We have used this finding to convert our $L_{\rm [O\,I]LVC}$–$L_{\rm acc}$ relation into an $L_{\rm [O\,I]LVC}$–$L_{\rm FUV}$ relation:

$$\log L_{\rm [O\,I]LVC} = (0.63 \pm 0.09) \times \log L_{\rm FUV} - (2.94 \pm 0.21). \quad (3)$$

Higher accreting stars have higher FUV luminosities and higher [O I] LVC luminosities. This positive correlation between stellar FUV luminosities and [O I] luminosities hints to the [O I] being a product of OH dissociation by FUV photons (Gorti et al. 2011).

The photodissociation of OH into hydrogen and oxygen atoms occurs when the molecule absorbs a photon with energy higher than 4.47 eV ($\lambda = 2616$ Å; van Dishoeck & Dalgarno 1984). About 50% of the time OH photodissociates to produce O in the ^1D state, and 5% in the higher ^1S state (Festou & Feldman 1981; Gorti et al. 2011 for a detailed explanation). The $^1D - {}^3P$ transition produces the oxygen doublet at $\lambda 6300$ and $\lambda 6363$, and the ^1S–^1D transition produces the emission at $\lambda 5577$.

---

[9] Note that S CrA N is marked as a green diamond in the next figures and is not included in the correlations due to the large contamination of the HVC to the LVC.
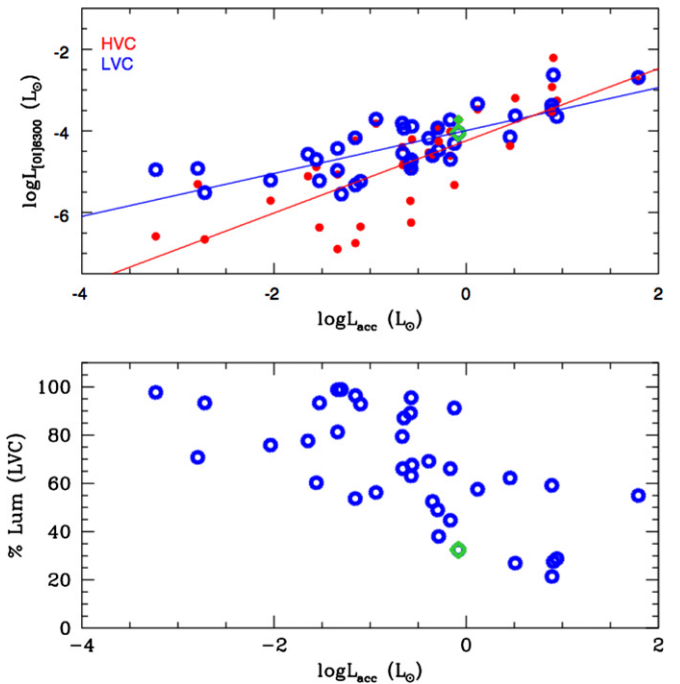

Figure 6. Top panel: [O I] luminosity vs. $L_{\rm acc}$. Different colors refer to different components: blue open symbols refer to the LVC; red filled small circles refer to the HVC. Bottom panel: percentage of the [O I] LVC compared to the total [O I] luminosity as a function of $L_{\rm acc}$. The green diamond represents S CrA N, which has not been considered in computing the relationship between $\log L_{\rm [O\,I]LVC} - \log L_{\rm acc}$ and $\log L_{\rm [O\,I]HVC} - \log L_{\rm acc}$ shown as blue and red solid lines, respectively.

(A color version of this figure is available in the online journal.)

The photodissociation of H_2O occurs via two main channels. In 79% of the cases, a water molecule dissociates into OH+H, and in the remaining 21% of the cases, O+2H are produced (Harich et al. 2001). The latter case requires a threshold energy of the FUV photon of about 9.5 eV to produce oxygen in the electronic ground state. The fraction of the oxygen atoms that are produced in the electronically excited D state is not known precisely, but Harich et al. (2001) argue that it is not a major channel even for energetically allowed FUV photons with energies greater than about 11.5 eV.

Since most H_2O photodissociates to OH, and this is generally followed by OH photodissociation to oxygen, there are about equal numbers of H_2O and OH photodissociations. However, since H_2O only photodissociates to oxygen 21% of the time and rarely produces oxygen in the ^1D state, the production of oxygen, of O^1D, and therefore of [O I] $\lambda 6300$ is primarily by the photodissociation of OH.

We next make a simple calculation to show that the FUV luminosity is sufficient to produce the observed [O I] via OH photodissociation, as suggested by the low $\lambda 6300/\lambda 5577$ ratios described in the next section. This calculation is done under the assumption that OH dominates the FUV opacity, and therefore absorbs all FUV photons that hit the disk. If $\dot N_{\rm OH}$ is the number of FUV photons photodissociating an OH molecule per second, about half of these produce an O^1D atom in an excited state that then radiatively decays. Therefore, $L_{\rm [O\,I]} \sim 1/2\,\dot N_{\rm OH} \times (hc/\lambda)$, where $hc/\lambda \sim 2$ eV is the energy of the $\lambda 6300$ photon. We make the assumption that Lyα photons dominate the FUV flux (e.g., Bergin et al. 2003) and that a fraction f_d of the stellar FUV flux is intercepted by the disk. We thus estimate that $\dot N_{\rm OH} \sim f_d \times (L_{\rm FUV}/10$ eV). Typically, $f_d \sim 0.5$. We therefore find that $L_{\rm [O\,I]} \sim 0.05\ L_{\rm FUV}$ is the maximum [O I] luminosity

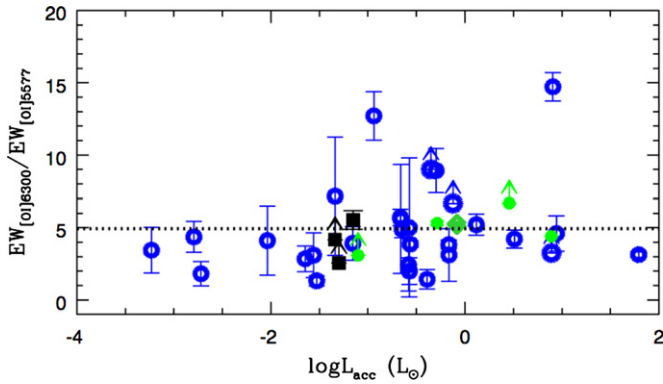**Figure 7.** EW [O I] $\lambda6300/\lambda5577$ ratios vs. log $L_{\rm acc}$. Sample I objects are shown as black squares (objects with an [Ne II] wind) and green filled circles (objects with a CO wind). The green diamond represents S CrA N. Sample II objects are shown as blue open circles. The black dotted line represents the mean value measured neglecting the lower limits.

(A color version of this figure is available in the online journal.)

Figure 8. FWHM vs. sine of the disk inclination. The blue open circles refer to a subsample of objects analyzed by HEG. The black squares refer to the Sample I objects with evidence of [Ne II] emission. The green filled circles are for the Sample I objects with evidence of CO emission.

(A color version of this figure is available in the online journal.)

that can be produced by OH if it dominates the FUV opacity. This is consistent with the measured relation between $L_{\rm [O I]}$ and $L_{\rm FUV}$; in other words, the observed $L_{\rm [O I]}$ are lower than the ones estimated in our simple calculation.

3.2.2. [O I] LVC Line Ratio

As discussed in Section 1, the low [O I] $\lambda6300/\lambda5577$ line ratio of 7 found for TW Hya (Pascucci et al. 2011) needs thermal emission coming from a very hot ($T \sim 5000$–8000 K) and dense ($n_e \sim 10^7$–10^8 cm^{-3}; $n_H \sim 10^8$–10^9 cm^{-3}) gas (Kwan & Tademaru 1995; Gorti et al. 2011). These physical conditions are unlikely in disks, especially in the photoevaporative flow. Such a low ratio can, however, be obtained from OH dissociation by FUV photons (Storzer & Hollenbach 1998). OH photodissociation results in [O I] $\lambda6300/\lambda5577$ line ratios that can range from ~7 to lower values depending on the density of the molecular gas (e.g., van Dishoeck & Dalgarno 1984; Gorti et al. 2011). Here we show that low ratios are typical in TTSs. Figure 7 presents the [O I] LVC $\lambda6300/\lambda5577$ EW ratios as a function of $L_{\rm acc}$ for our Sample I and Sample II sources. We find that these ratios range between ~1 and ~8, with a mean value of ~5, and change very little over six orders of magnitude in $L_{\rm acc}$. There are two exceptions in our samples: DGTau and HNTau, which have ratios of ~15 and ~13, respectively. Both sources power a strong jet (HEG and Hartigan et al. 2004), which makes it difficult to reliably estimate the EW of the LVC, especially in the $\lambda6300$ line. The higher ratio may reflect a contamination of the HVC in the $\lambda6300$ line profile, or indicate a higher contribution from thermal emission in these cases. There are seven lower limits to the $\lambda6300/\lambda5577$ EW ratio due to non-detections of the [O I] $\lambda5577$ line. These lower limits span over the entire EW ratio covered by the detections and do not allow us to draw any further conclusion.

3.2.3. FWHM and Peak Velocities of the LVC

FWHMs and peak velocities provide useful information about the gas kinematics. We list these quantities for our Sample I and for the subset of Sample II objects where the LVC and the HVC can be well separated in Table 4. As mentioned in Section 2.5, we have selected only Sample II objects with an LVC that is clearly distinct from the HVC (see HEG's Tables 8, and Table 4 in this paper for the complete Sample I and II sources used in this analysis). As described in Section 3.1, we
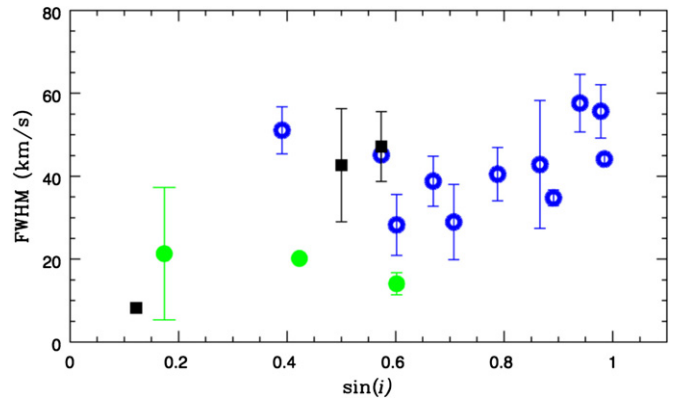
measure peak velocities and FWHMs to characterize, to a first order, the profiles of the [O I] $\lambda6300$ line. However, for S CrA N, RU Lup, and V866 Sco (marked with an asterisk in Table 4), we opted to use the [O I] $\lambda5577$ line because the $\lambda6300$ LVC is contaminated by the HVC (see Figure 1).

Figure 8 shows that the FWHMs range between 10 and 60 km s^{-1} (with the only exception of SCrA N, which exhibits an FWHM ~ 110 km s^{-1}; see Table 4), with several sources clustering around ~40 km s^{-1}. The FWHMs measured for the samples analyzed here are larger than that predicted by models of EUV/X-ray photoevaporation (Ercolano & Owen 2010). Moreover, the median FWHM suggests an origin in the inner part of the disk (~0.5 AU) under the assumption of Keplerian rotation.

In Table 4, we report the peak centroids (with respect to the star velocity). They span between +1 km s^{-1} and ~ -10 km s^{-1}, the mean being -5.0 km s^{-1}. The exceptions are SCrA N for Sample I and YY Ori and DQ Tau for Sample II objects, where the largest blueshifts indicate a contamination from the HVC. Blueshifts in the [O I] LVC were already noted by HEG and are a clear signature of unbound gas flowing outward, the redshifted gas being occulted by the disk.

Figure 8 shows a *possible* trend of increasing FWHM with increasing disk inclination. This can be explained by bound gas in Keplerian rotation around the star. At the same time, the blueshifts in peak velocities should trace unbound gas. This suggests that the [O I] LVC may itself have multiple components. This hint is corroborated by the analysis of the highest resolution and S/N spectra (see Section 3.2.4). We have also searched for but not found any clear trend between the FWHM or peak velocity and the stellar accretion luminosity.

3.2.4. Two-component Fit to the LVC

Here, we investigate the possibility that the [O I] LVC can itself have multiple components. For this purpose, we have chosen the two stars among the Sample I objects with S/N ratio around the [O I] lines higher than 100, and with the higher resolution, namely, V866 Sco (seen at an inclination of 25°) and DR Tau (seen at 37°). Figure 9 shows the $\lambda5577$ line for V866 Sco and the [O I] $\lambda6300$ line for DR Tau, both enlarged to show the ±100 km s^{-1} velocity range. The first choice is motivated by the fact that an HVC is present in the [O I] $\lambda6300$ spectrum of V866 Sco (see Figure 1) and we want to minimize
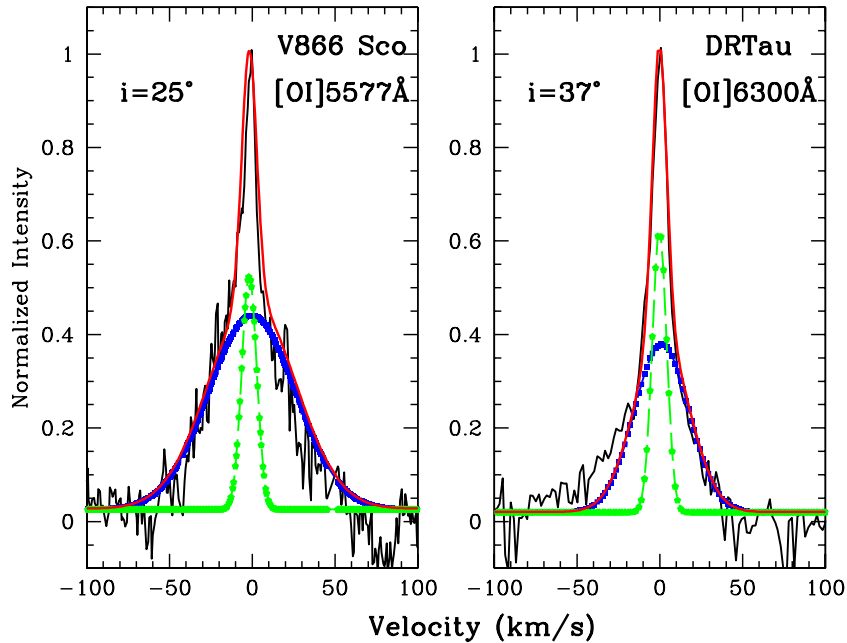
Figure 9. Double Gaussian fit for the DR Tau and V866 Sco line profiles. Black: observed profile; red: summed profile; green: narrow-component LVC; and blue: broad-component LVC.

(A color version of this figure is available in the online journal.)

Table 5
Narrow Component (NC) and Broad Component (BC) of the LVC

Star	FWHM[a] BC-LVC	v_{peak}[a] BC-LVC	FWHM[a] NC-LVC	v_{peak}[a] NC-LVC	$Area$ BC[b] (%)
DR Tau	40.7	−0.2	9.8	−0.1	38%
V866 Sco	61.9	−0.1	10.7	−1.8	45%

Notes.
[a] FWHM and v_{peak} are in km s^{-1}.
[b] Percentage of the area covered by the BC.

any contamination by the HVC in this analysis. Unfortunately, the [O I] λ5577 line is not detected in the high-resolution UVES spectrum of DR Tau so we analyze here the [O I] λ6300 profile.

The profiles in Figure 9 show a broad-based emission and a narrow-peaked core. We therefore use two Gaussian profiles to fit the LVC: a narrow component (NC-LVC) to reproduce the central peaked emission and a broad component (BC-LVC) to account for the broader wing emission.

We define the range of velocities where the NC-LVC peaks and leave the Gaussian parameters (namely amplitude, width, and peak centroid) free to vary. Then, we fit a Gaussian profile over the total minus best-fit NC-LVC profile. The total line profile (plotted in red in Figure 9) is the sum of the two Gaussian profiles (green is the NC-LVC and blue is the BC-LVC). The FWHMs and peak velocities for both components are reported in Table 5.

We find that the spectrum of V866 Sco is well reproduced by two Gaussians: a broad component centered at ∼0 km s^{-1}, and a narrow component blueshifted by −1.8 km s^{-1}. The BC-LVC has an FWHM that is about a factor of six larger than that of the NC-LVC and contributes about half of the flux.

In the case of DR Tau, our procedure finds that two Gaussians centered around 0 km s^{-1} can reproduce the total LVC observed profile. However, there is a residual weak but extended blue wing that is not fitted by the sum of the two Gaussians. This excess

emission could be a contamination from the HVC. More high-resolution spectra are needed to definitively address this point. For both objects, the errors on the peak velocity are ∼0.7 km s^{-1}, as listed in Table 4.

We find that the FWHM of the whole LVC is larger than that found for the NC-LVC. For both sources, the NC-LVC is reduced to ∼10 km s^{-1}, from 20 km s^{-1} for V866 Sco and 14 km s^{-1} for DR Tau.

4. OBSERVATIONAL CONSTRAINTS ON THE ORIGIN OF THE [O I] LVC

Our observations and analysis provide four distinct constraints on the origin of the [O I] LVC.

1. Our comparison of [Ne II], [O I], and CO line profiles hints at a trend between their peak velocities, with the [Ne II] line being more blueshifted than the [O I] line, which in turn is more blueshifted than the CO line. The average [Ne II] peak velocity is ∼−8 km s^{-1} (Sacco et al. 2012), the median of the [O I] LVC is −5 km s^{-1} (this work and HEG), while the shifts in the CO line are <5 km s^{-1} and may not be significant given the associated uncertainties (Bast et al. 2011). The X-EUV disk models of Ercolano & Owen (2010) predict that [O I] lines should have a larger blueshift than [Ne II] lines in primordial (not gapped) disks. This is because in their models the [O I] emitting region resides in hotter gas closer to the star and above the [Ne II] emitting region. As an example, Ercolano & Owen (2010) predict shifts of −6 and −3 km s^{-1} for the [O I] and [Ne II] line centroids, respectively, for a disk inclined by 40°. This trend is opposite to what we see in the data, suggesting that the [O I] emitting region is at larger disk radii or deeper in the disk than the [Ne II] emitting region. The broader [O I] and CO profiles with respect to the [Ne II] line suggest a larger contribution from bound inner disk gas for [O I] and CO.

2. We measure [O I] $\lambda6300$ LVC line luminosities ranging from 10^{-3} to 10^{-6} $L_\odot$, with a mean value of 4.5×10^{-5} $L_\odot$. While these large values exclude emission from the EUV fully ionized layer, they are consistent with [O I] tracing either thermal excitation in the soft X-ray-heated region (Hollenbach & Gorti 2009; Ercolano & Owen 2010) or non-thermal excitation in regions where OH is photodissociated by FUV photons into oxygen atoms in excited electronic states (Gorti et al. 2011). However, the lack of correlation between the [O I] luminosity and L_X and the positive tight correlation with L_{acc} (L_{FUV}) seem to favor the latter over the first scenario (Section 3.2.1). We are cautious not to draw a stronger conclusion based solely on this observable because the measured L_X may miss the soft-X-ray component, which, if present, may still irradiate the disk surface and heat it sufficiently to produce thermal [O I] emission. Hints that evolved transitional disks may "see" this soft X-ray component come from line ratios of ionic species detected at infrared wavelengths (Szulágyi et al. 2012). However, in classical disks, accreting at perhaps higher rates than transitional disks (Espaillat et al. 2012; Kim et al. 2013), the situation may be different. Strongly accreting sources are known to be accompanied by mass outflows (10–100 times lower than accretion rates; Cabrit et al. 1990; HEG), and Hollenbach & Gorti (2009) calculate that soft X-rays will not penetrate the outflow column to irradiate the disk when $\dot{M}_{acc}$ is $\gtrsim 10^{-9}$ $M_\odot$ yr^{-1}. The majority of the stars analyzed here have $L_{acc} > 10^{-2}$ $L_\odot$ (see Figure 5), meaning $\dot{M}_{acc} \gtrsim 10^{-9}$ $M_\odot$ yr^{-1}. Therefore, outflows could absorb most of the soft X-ray component from the star. FUV photons, on the other hand, can penetrate the outflow column and reach the disk surface for $\dot{M}_{acc} \lesssim 4 \times 10^{-7}$ $M_\odot$ yr^{-1}, basically for all but four stars in our sample. The FUV photon luminosity is high enough for [O I] photodissociation to explain the observed [O I] LVC luminosities. In the framework of the FUV model, the correlation shown in Equation (3) can be easily explained because more FUV stellar photons impinging on the disk imply more OH dissociation and hence higher [O I] luminosities.

3. We measure [O I] $\lambda6300$/[O I] $\lambda5577$ line ratios for a large sample of TTSs and find values ranging from $\sim$1 to $\sim$8 over six orders of magnitude in L_{acc}. These small values are difficult to produce in thermally heated gas present on the surface of protoplanetary disks but can be explained in a disk layer where [O I] is produced by the non-thermal process of OH dissociation by FUV photons (Gorti et al. 2011). This observable independently points to [O I] optical emission tracing stellar FUV photons impinging on the disk (see constraint 2).

4. The measured FWHMs are larger than those predicted by the models accounting for disk photoevaporation. These larger FWHMs suggest an origin of the line in the inner part of a disk in Keplerian rotation. Moreover, we find a possible trend of increasing FWHM of the [O I] LVC with increasing disk inclination (Figure 8). This correlation can be explained again by bound gas in Keplerian rotation around the star. At the same time, we confirm the average blueshift of -5 km s^{-1} found by HEG. This suggests the presence of multiple components within the [O I] LVC. A detailed analysis of the [O I] profiles for the two highest resolution and S/N spectra confirms this notion. The spectrum of V866 Sco is well reproduced by two Gaussians: a broad component centered at $\sim$0 km s^{-1} and a narrow component blueshifted by $\sim$$-2$ km s^{-1}. The BC-LVC could trace bound disk gas in Keplerian rotation around the star. Its broad FWHM of $\sim$60 km s^{-1} points to [O I] gas as close in as $\sim$0.2 AU. If the BC-LVC profile lacks a double peak (which cannot be proven by these data due to contamination of the NC-LVC), then gas should extend out to $\sim$10 AU.[10] The BC-LVC contributes to about 40% of the total flux (Table 5). In the case of DR Tau, the observed spectrum is reproduced by two Gaussians centered around 0 km s^{-1}, even if this configuration cannot reproduce the excess emission on the blue side of the [O I] $\lambda6300$ profile. This excess emission contributes to less than 10% of the total [O I] LVC emission and could either be a wind component or contamination by the HVC. The FWHM of the BC-LVC is $\sim$40 km s^{-1} and points to [O I] gas as close in as $\sim$0.6 AU. In both the sources, the FWHM of the NC-LVC is $\sim$10 km s^{-1}. This component may be associated with that portion of the [O I] gas that becomes gravitationally unbound at radial distances $\geqslant$10 AU. For gas heated to $T \sim$ 1000 K by FUV or hard X-ray photons, the sound speed is $\sim$2 km s^{-1}, corresponding to the blueshift found for the NC-LVC of V866 Sco. The average blueshift found for the sample analyzed here and by HEG is larger, $\sim$5 km s^{-1}. Our blueshifts may be consistent with a mainly molecular photoevaporative wind, but given the uncertainties, the origin of the NC-LVC cannot be pinned down.

The ensemble of data presented here supports the following scenario for the origin of the [O I] LVC. Stellar FUV photons penetrate the outflow columns of classical TTSs and reach the disk surface where they dissociate OH molecules, resulting in oxygen atoms in the ^1D and ^1S states. The atoms then decay to the ground state via the [O I] $\lambda6300$ and $\lambda5577$ lines. Higher accretion rates imply higher FUV luminosities, higher rates of OH dissociation, and hence higher [O I] luminosities as observed. This photodissociated layer may have a bound component of gas in Keplerian rotation and unbound gas at radial distances $\geqslant$10 AU, likely a photoevaporative wind. This wind is heated by either the same FUV photons that dissociate OH molecules or by hard ($>$1 keV) X-ray photons that can also penetrate the outflow column. These hard X-ray photons may be responsible for producing the [Ne II] blueshifted emission from gas at higher vertical heights of the accelerating photoevaporative flow.

Distinguishing the bound from the unbound component and determining the wind-driving agent is key to measuring photoevaporative mass-loss rates. If FUV driven, one might expect that the peak of the flowing component (NC-LVC) correlates with the FUV luminosity (more FUV would lead to higher temperature, and the higher the temperature, the faster the flow, hence the larger the blueshifts). In this case, the FUV radiation is not only photodissociating the OH molecules but also driving the flow. On the other hand, if the flow is X-ray driven, one might expect a correlation between the peak centroids of the NC-LVC and the X-ray luminosity. In this case, the [O I] is produced by the FUV photodissociation of the OH molecules, but X-ray photons heat and launch this molecular flow. Since the hard X-ray flux is well determined, we searched for trends between v_{peak} and L_X for our sample. We found no correlation with L_X (correlation coefficient $\sim$0.01) and only a

---

[10] We also tested Keplerian profiles for the BC-LVC and found that double-peaked Keplerian profiles resulted in less good fits than single-peaked Keplerian profiles.

weak correlation with $L_{\rm FUV}$ (correlation coefficient ~-0.33), and therefore cannot make any strong conclusions. A larger sample of high-resolution spectra is required to decide between the two mechanisms driving the wind.

As disks evolve and mass accretion rates decline below $\dot{M}_{\rm acc}$ $\lesssim 10^{-9}\,M_\odot$ yr^{-1}, EUV (and soft X-rays) can start penetrating the outflow columns, and EUV photons rather than X-rays may be responsible for producing [Ne II] emission in these disks. The lack of blueshift in the [O I] line from the evolved disk of TW Hya (Pascucci et al. 2011) is consistent with our scenario. In this case, the bound [O I] component dominates and there is no detectable unbound component. Given the lower mass accretion rate of this star (lower FUV photon flux) and the less flared disk surface with respect to that of classical T Tauri disks (Gorti et al. 2011), FUV or X-rays may be inefficient in driving a dense molecular photoevaporative wind. Extrapolating our scenario to disks around stars with higher mass accretion rates than classical TTSs, we should expect a decline in the [O I] LVC as fewer stellar FUV photons can penetrate more massive winds. Indeed, for the Class I/Class II stars in Taurus–Auriga from the sample of White & Hillenbrand (2004), we note that while the [O I] LVC in their optical spectra is always detected in Class II objects, it is missing in some Class I objects (e.g., L1551-IRS5, HLTau).

5. SUMMARY

To understand the origin of the [O I] LVC, we analyzed archival high-resolution optical spectra for two samples of objects: (1) a sample of stars with previously detected [Ne II] 12.81 μm and/or CO rovibrational 4.7 μm emission and with profiles suggestive of a slow disk wind, and (2) the comprehensive survey of classical TTSs in Taurus collected by HEG.

Our comparison of [O I] LVC profiles with the [Ne II] and CO profiles identifies a possible trend in peak centroids with the [Ne II] being more blueshifted than the [O I], which, in turn, is more blueshifted than the CO line. In addition, the broader profiles of the [O I] and CO with respect to the [Ne II] line point to the presence of more bound gas contributing to the [O I] and CO emission. These results are consistent with the three gas diagnostics tracing different parts of a photoevaporative flow, with the [Ne II] being likely in the top layer.

We discover a correlation between the luminosity of the [O I] LVC and stellar accretion rates ($L_{\rm acc}$), which we consistently compute for the Sample I and II objects. Because $L_{\rm acc}$ is known to positively correlate with the stellar FUV luminosity, our result implies that the higher the stellar FUV luminosity, the higher is the [O I] luminosity of the LVC. The correlation with ($L_{\rm acc}$) and the [O I] luminosity of the LVC implies that if there is an unbound component to the LVC from a photoevaporative flow, the flow is stronger for stars with higher accretion rates. This is in contrast to the usual assumption that photoevaporation is only important in late-stage disk evolution. Instead, it may be proceeding throughout the T Tauri phase, at rates that decrease as the accretion rate decreases.

We also show that the [O I] $\lambda6300/\lambda5577$ EW ratios span only a narrow and low range of values (1–8) over six orders of magnitude in $L_{\rm acc}$ and most likely are a result of OH photodissociation. We measure larger FWHMs than those predicted by the photoevaporating models and find a trend of increasing FWHM with increasing disk inclinations for the [O I] LVC, which points to bound gas in Keplerian rotation around the star. At the same time, the average -5 km s^{-1} peak velocity points to an unbound gas component.
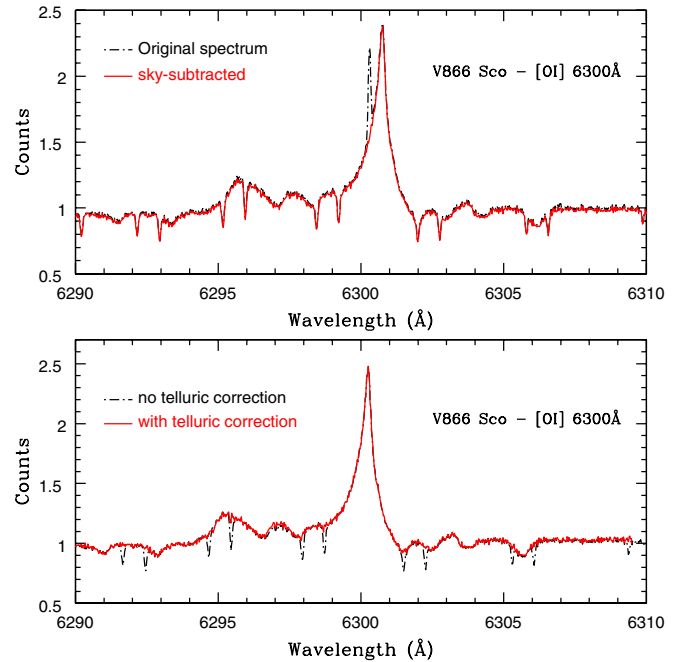

Figure 10. V866 Sco in the region around the [O I] $\lambda6300$ line. Top panel: original spectrum (dashed, black profile) and sky-subtracted spectrum (solid, red profile). The profiles are corrected for the heliocentric velocity but not for the radial velocity of the star. Bottom panel: spectrum of the target star with no correction for the telluric features (dashed, black profile) and after telluric correction (solid, red line). The profiles in this panel are in the stellocentric reference frame. All the spectra presented in this paper have been corrected for terrestrial emission and absorption features.

(A color version of this figure is available in the online journal.)

The analysis of the two highest resolution and signal-to-noise spectra shows that indeed the [O I] LVC traces at least two different components: bound disk gas in Keplerian rotation and unbound gas farther out ($\geqslant 10$ AU). Higher resolution spectra on a larger sample of disks are necessary to test our inference of multiple LVC components and their ubiquity.

Our results demonstrate that a thermal origin of the [O I] in an X-ray-heated photoevaporative wind, as proposed by Ercolano & Owen (2010), has several shortcomings. It cannot explain the trend in peak velocities between [Ne II] and [O I] lines and cannot easily account for (1) the lack of correlation between the [O I] luminosity and L_X, (2) the correlation of $L_{\rm [O I]}$ and $L_{\rm FUV}$ extending beyond mass flow rates that should block soft X-ray photons, and (3) the low [O I] $\lambda6300/\lambda5577$ line ratios. Based on our analysis, we propose an alternative scenario in which the [O I] LVC traces the disk layer where stellar FUV photons dissociate OH molecules in oxygen and hydrogen atoms. Part of this layer may participate in a photoevaporative wind that could be driven either by FUV or by hard X-ray photons.

A larger sample of high-resolution spectra is definitively required to decide between the two mechanisms driving the wind.

APPENDIX

We report in Figure 10 the reduction steps applied to the spectrum of V866 Sco.

REFERENCES

Acke, B., van den Ancker, M. E., & Dullemond, C. P. 2005, A&A, 436, 209
Alencar, S. H. P., & Batalha, C. 2002, ApJ, 571, 378
Andrews, S. M., Wilner, D. J., Hughes, A. M., et al. 2010, ApJ, 723, 1241
Baldovin-Saavedra, C., Audard, M., Carmona, A., et al. 2012, A&A, 543, 30
Bast, J. E., Brown, J. M., Herczeg, G. J., van Dishoeck, E. F., & Pontoppidan, K. M. 2011, A&A, 527, A119
Bergin, E., Calvet, N., D'Alessio, P., & Herczeg, G. J. 2003, ApJ, 591, 159
Beristain, G., Edwards, S., & Kwan, J. 2001, ApJ, 551, 1037
Brown, J., Pontoppidan, K., van Dishoeck, E., et al. 2013, ApJ, 770, 94
Cabrit, S., Edwards, S., Strom, S. E., & Strom, K. M. 1990, ApJ, 354, 687
Calvet, N., Hartmann, L., & Strom, S. E. 2000, in Protostars and Planets IV, ed. V. Mannings, A. P. Boss, & S. S. Russell (Tucson, AZ: Univ. Arizona Press), 377
Clarke, C. J., Gendrin, A., & Sotomayor, M. 2001, MNRAS, 328, 485
Close, L. M., Dutrey, A., Roddier, F., et al. 1998, ApJ, 499, 883
Cortes, S. R., Meyer, M. R., Carpenter, J. M., et al. 2009, ApJ, 697, 1305
Curran, R. L., Argiroffi, C., Sacco, G. G., et al. 2011, A&A, 526, 104
Davis, C. J., Eislöffel, J., & Smith, M. D. 1996, ApJ, 463, 246
Donati, J. F., Gregory, S. G., Montmerle, T., et al. 2011, MNRAS, 417, 1747
Edwards, S., Cabrit, S., Ghandour, L. O., & Strom, S. E. 1989, in ESO Workshop Proc. 33, Low-Mass Star Formation and Pre-Main-Sequence Objects, ed. B. Reipurth (Garching: ESO), 385
Ercolano, B., Clarke, C. J., & Drake, J. J. 2009, ApJ, 699, 1639
Ercolano, B., & Owen, J. E. 2010, MNRAS, 406, 1553
Espaillat, C., Ingleby, L., Hernàndez, J., et al. 2012, ApJ, 747, 103
Fang, M., van Boekel, R., Wang, W., et al. 2009, A&A, 504, 461
Ferreira, J., Dougados, C., & Cabrit, S. 2006, A&A, 453, 785
Festou, M., & Feldman, P. 1981, A&A, 103, 154
Fischer, W., Edwards, S., Hillenbrand, L., & Kwan, J. 2011, ApJ, 730, 73
Font, A. S., McCarthy, I. G., Johnstone, D., & Ballantyne, D. R. 2004, ApJ, 607, 890
Furlan, E., Hartmann, L., Calvet, N., et al. 2006, ApJS, 165, 568
Ghez, A. M., McCarthy, D. W., Patience, J. L., & Beck, T. L. 1997a, ApJ, 481, 378
Ghez, A. M., Neugebauer, G., & Matthews, K. 1993, AJ, 106, 2005
Ghez, A. M., White, R. J., & Simon, M. 1997b, ApJ, 490, 353
Gorti, U., Hollenbach, D., Najita, J., & Pascucci, I. 2011, ApJ, 735, 90
Güdel, M., Briggs, K. R., Arzner, K., et al. 2007, A&A, 468, 353
Güdel, M., Lahuis, F., Briggs, K. R., et al. 2010, A&A, 519, A113
Guilloteau, S., Dutrey, A., Pietu, V., & Boehler, Y. 2011, A&A, 529, 105
Gullbring, E., Hartmann, L., Briceno, C., & Calvet, N. 1998, ApJ, 492, 323
Hamann, F. 1994, ApJS, 93, 485
Harich, S. A., Huang, D. W., Yang, X. F., et al. 2001, JChPh, 114, 7830
Hartigan, P., Edwards, S., & Ghandour, L. 1995, ApJ, 452, 736 (HEG)
Hartigan, P., Edwards, S., & Pierson, R. 2004, ApJ, 609, 261
Hartigan, P., Kenyon, S. J., Hartmann, L., et al. 1991, ApJ, 382, 617
Herczeg, G., & Hillenbrand, L. 2008, ApJ, 681, 594
Herczeg, G. J., Walter, F. M., Linsky, J. L., et al. 2005, AJ, 129, 2777
Hillenbrand, L. 2008, PhST, 130, 4024
Hirth, G. A. 1994, in ASP Conf. Proc. 57, Stellar and Circumstellar Astrophysics, ed. G. Wallerstein & A. Noriega-Crespo (San Francisco, CA: ASP), 32
Hirth, G. A., Mundt, R., & Solf, J. 1997, A&AS, 126, 427

Hollenbach, D., & Gorti, U. 2009, ApJ, 703, 1203
Hollenbach, D., Yorke, H. W., & Johnstone, D. 2000, in Protostars and Planets IV, ed. V. Mannings, A. P. Boss, & S. S. Russell (Tucson, AZ: Univ. Arizona Press), 401
Isella, A., Carpenter, J., & Sargent, A. 2009, ApJ, 701, 260
Kastner, J. H., Hily-Blant, P., Sacco, G. G., Forveille, T., & Zuckerman, B. 2010, ApJL, 723, L248
Kastner, J. H., Zuckerman, B., Hily-Blant, P., & Forveille, T. 2008, A&A, 492, 469
Kim, K. H., Watson, D. M., Manoj, P., et al. 2013, ApJ, 769, 149
Kitamura, Y., Momose, M., Yokogawa, S., et al. 2002, ApJ, 581, 357
Königl, A., & Pudritz, R. E. 2000, in Protostars and Planets IV, ed. V. Mannings, A. P. Boss, & S. S. Russell (Tucson, AZ: Univ. Arizona Press), 759
Königl, A., & Salmeron, R. 2011, in Physical Processes in Circumstellar Disks around Young Stars, ed. P. J. V. Garcia (Chicago: Univ. Chicago Press), 283
Kwan, J., & Tademaru, E. 1995, ApJ, 454, 382
Luhman, K. L. 1999, ApJ, 525, 466
Luhman, K. L. 2007, ApJS, 173, 104
Lynden-Bell, D., & Pringle, J. E. 1974, MNRAS, 168, 603
Mathieu, R. D., Stassun, K., Basri, G., et al. 1997, AJ, 113, 1841
Mathis, J. 1990, ARA&A, 28, 37
Meijerink, R., Glassgold, A. E., & Najita, J. R. 2008, ApJ, 676, 518
Melo, C. H. F. 2003, A&A, 410, 269
Muzerolle, J., Hillenbrand, L., Calvet, N., et al. 2003, ApJ, 592, 266
Najita, J., Carr, J. S., & Mathieu, R. D. 2003, ApJ, 589, 931
Owen, J. E., Ercolano, B., Clarke, C. J., & Alexander, R. D. 2010, MNRAS, 401, 1415
Panoglou, D., Cabrit, S., Pineau des Forets, G., et al. 2012, A&A, 538, 2
Pascucci, I., Apai, D., Hardegree-Ullman, E. E., et al. 2008, ApJ, 673, 477
Pascucci, I., & Sterzik, M. 2009, ApJ, 702, 724
Pascucci, I., Sterzik, M., Alexander, R. D., et al. 2011, ApJ, 736, 13
Petrov, P. P., Gahm, G. F., Stempels, H. C., et al. 2011, A&A, 535, 6
Pietu, V., Gueth, F., Hily-Blant, P., et al. 2011, A&A, 528, 81
Pontoppidan, K. M., Blake, G. A., & Smette, A. 2011, ApJ, 733, 84
Prato, L., Greene, T. P., & Simon, M. 2003, ApJ, 584, 853
Qi, C., Ho, P. T. P., Wilner, D., et al. 2004, ApJ, 616, 11
Reipurth, B., & Zinnecker, H. 1993, A&A, 278, 81
Rigliaco, E., Natta, A., Testi, L., et al. 2012, A&A, 548, 56
Sacco, G. G., Flaccomio, E., Pascucci, I., et al. 2012, ApJ, 747, 142
Salyk, C., Blake, G. A., Boogert, A. C. A., & Brown, J. M. 2011, ApJ, 743, 112
Shu, F. H., Najita, J., Shang, H., & Li, Z. Y. 2000, in Protostars and Planets IV, ed. V. Mannings, A. P. Boss, & S. S. Russell (Tucson, AZ: Univ. Arizona Press), 789
Siess, L., Dufour, E., & Forestini, M. 2000, A&A, 358, 593
Silber, J., Gledhill, T., Duchene, G., & Mènard, F. 2000, ApJ, 536, 89
Stelzer, B., & Neuhäuser, R. 2001, A&A, 377, 538
Stempels, H. C., & Gahm, G. F. 2004, A&A, 421, 1159
Stempels, H. C., Gahm, G. F., & Petrov, P. P. 2007, A&A, 461, 253
Stempels, H. C., & Piskunov, N. 2002, A&A, 391, 595
Stempels, H. C., & Piskunov, N. 2003, A&A, 408, 693
Storzer, H., & Hollenbach, D. 1998, ApJ, 502, 71
Szulagyi, J., Pascucci, I., Abraham, P., et al. 2012, ApJ, 759, 47
Takami, M., Bailey, J., Gledhill, T. M., Chrysostomou, A., & Hough, J. H. 2001, MNRAS, 323, 177
van Boekel, R., Güdel, M., Henning, T., Lahuis, F., & Pantin, E. 2009, A&A, 497, 137
van Dishoeck, E. F., & Dalgarno, A. 1984, Icar, 59, 305
Weaver, B. W. M. 1986, PASP, 98, 1109
White, R. J., & Ghez, A. M. 2001, ApJ, 556, 265
White, R. J., & Hillenbrand, L. A. 2004, ApJ, 616, 998
Yang, H., Herczeg, G. J., Linsky, J. L., et al. 2012, ApJ, 744, 121